Chemical and electrochemical surface modification and fatigue response of PBF-LB/M 316L stainless steel

Citation for the original published paper (version of record):
Manchili, S., Pezzotti, C., Dartfeldt, E. et al (2026). Chemical and electrochemical surface
modification and fatigue response of PBF-LB/M 316L
stainless steel. Progress in Additive Manufacturing, In Press.
http://dx.doi.org/10.1007/s40964-025-01482-x

Progress in Additive Manufacturing
https://doi.org/10.1007/s40964-025-01482-x

RESEARCH

Chemical and electrochemical surface modification and fatigue response of PBF-LB/M 316L stainless steel

Swathi Kiranmayee Manchili[1] · **Fabio Pezzotti**[1] · **Erik Dartfeldt**[1] · **Martina Halmdienst**[2] · **Uta Klement**[3] · **Seyed Hosseini**[4,5]

Received: 16 July 2025 / Accepted: 12 December 2025

Abstract

Laser beam-powder bed fusion/metal (PBF-LB/M) offers significant advantages for manufacturing 316L stainless steel components. However, inherent surface roughness can limit their application in sectors requiring high-quality surfaces. This study investigates the influence of two electrochemical post-processing techniques, Hirtisation and DLyte, on surface topography and fatigue behavior of PBF-LB fabricated 316L stainless steel. Vertically built cylindrical fatigue specimens were subjected to both the treatments. Following surface treatment, surface roughness, residual stress, microstructure, and high-cycle fatigue properties were studied. Hirtisation significantly reduced the average surface roughness (S_a) around 70%, with a further improvement to around 80% after DLyte treatment. The mean roughness depth and deepest valley depth also decreased after post-processing. Notably, uniaxial fatigue testing revealed a 20% increase in fatigue life for specimens subjected to Hirtisation while around 40% for a combination treatment, Hirtisation + DLyte compared to the as-built condition. However, these specimens exhibited higher surface tensile residual stress levels. This suggests a trade-off between the benefits of a smoother surface (reduced fatigue crack initiation sites) and the detrimental effects of higher residual stress (promoting crack propagation). Despite the improvement in surface quality, the treated specimens exhibited higher surface residual stress, which may counteract some fatigue benefits.

Keywords Surface roughness · Fatigue behavior · Post-processing · Electrochemical treatment · Hirtisation® · DLyte

1 Introduction

Powder bed fusion-laser beam/metal (PBF-LB/M) is a widely adopted additive manufacturing (AM) technique for complex metal components [1]. Despite its advantages like design flexibility, as-built surface conditions present significant challenges for industrial application [2]. PBF-LB/M parts typically exhibit high surface roughness from adhering particles and tensile residual stresses from rapid solidification. These anomalies accelerate crack initiation and reduce fatigue life [3–5]. Consequently, effective post-processing is crucial to reduce defects, relieve stresses, and enhance part reliability and performance.

Surface finishing techniques for AM parts fall into four main categories: mechanical, surface melting, chemical, and electrochemical [6]. Each offers unique benefits and challenges depending on material, desired traits, and application. While mechanical and surface melting methods suit many parts, they struggle with AM's complex internal geometries and limited cooling paths. Chemical methods

---

✉ Swathi Kiranmayee Manchili
swathi.manchili@ri.se

Fabio Pezzotti
fabio.pezzotti@ri.se

Erik Dartfeldt
erik.dartfeldt@ri.se

Martina Halmdienst
martina.halmdienst@rena.com

Uta Klement
uta.klement@chalmers.se

Seyed Hosseini
seyed.hosseini@skf.com

[1] RISE Research Institutes of Sweden, Gothenburg, Sweden

[2] RENA Technologies (Germany), Gütenbach, Germany

[3] Department of Industrial and Materials Science, Chalmers University of Technology, Gothenburg, Sweden

[4] SKF (Sweden), Gothenburg, Sweden

[5] RISE Research Institutes of Sweden, Gothenburg, Sweden

Table 1 Chemical composition of 316L SS powder provided by Höganäs AB (wt%)

Fe	C	Mo	Ni	Mn	Cr	Si	O
Balance	0.015	2.5	12.7	1.5	16.9	0.7	0.059

Table 2 Process parameters employed

Parameter	Values
Laser power	200 W
Laser speed	800 mm/s
Hatch distance	0.12 mm
Rotation angle	67°
Laser spot size	65 µm
Stripe scan pattern	Stripes

excel for intricate internal areas due to fluid penetration [7]. Reviews highlight chemical polishing (CP) and electrochemical polishing (ECP) as most effective for enhancing internal surface quality, with electrochemical methods also ideal for accessible external surfaces due to their reliance on electric current flow [8, 9].

Innovative methods further refine surface control. Hirtisation® combines dynamic electrochemical and hydrodynamic processes, significantly reducing surface roughness (50–75% in Ti-6Al-4 V and AlSi10Mg) and improving fatigue behavior [2, 10, 11]. DryLyte, a patented dry electropolishing method using solid electrolytes, effectively removes oxides [12]. Research on 316L stainless steel showed that combining pre-grinding with DLyte reduced surface roughness (Ra) from ~ 10 µm to 0.13 µm, emphasizing the benefits of integrated finishing techniques [13].

This study examines how Hirtisation® and DLyte surface finishing affect the axial fatigue performance of 316L stainless steel parts made by PBF-LB/M. Samples were produced under identical optimized conditions to minimize porosity. The research covers material and fabrication details, surface topography, and residual stress analysis. Fatigue performance is evaluated across four surface finishes from different post-processing methods. Fractography reveals failure mechanisms linked to each finishing technique. The study concludes by explaining factors influencing fatigue strength, highlighting the effectiveness of Hirtisation® and DLyte treatments. Although a stress-relief heat treatment is commonly applied after PBF-LB/M to reduce residual stress and prevent distortion during post-processing, it was intentionally omitted in this study to isolate the specific effects of Hirtisation® and DLyte on surface quality and fatigue behaviour. The simple cylindrical geometry and uniform build layout minimized the risk of distortion.

2 Materials and experimental techniques

2.1 Powder material

To prepare the test samples, stainless steel powder 316L with the chemical composition given in Table 1 was used. The powder was manufactured by Höganäs AB, Sweden.

The powder had an apparent density of 4.09 g/cm^3 and a flow rate of 16 s/50 g. BET analysis showed a specific surface area of 0.030 m^2/g. Particle size distribution measured D10, D50, and D90 as 31, 45.4, and 65.9 µm, respectively [14]. Before use, the powder was dried at 60 °C for 24 h and sieved to enhance flowability and reduce impurities, ensuring consistent specimen quality for fatigue testing.

2.2 Printing and specimen fabrication

To ensure defect-free 316L stainless steel samples, optimized process parameters provided by the machine manufacturer were used for the fabrication of test geometries, as outlined in Table 2.

An SLM 125 HL system (Nikon SLM Solutions GmbH, Germany) equipped with a single 400 W fibre laser was used to fabricate 316L specimens via PBF-LB process, operating within a build envelope of 125 × 125 x 125 mm^3. Optimized manufacturer parameters (316L_SLM_MBP3.0_30_CE1_400W_Stripes_V1.1) were used to minimize defects, as outlined in Table 2. Specimens were built directly on the plate with the build direction aligned to their length, using a contour-first strategy with two border scans and one fill. Sixty fatigue test specimens were produced in standard cylindrical geometry (Fig. 1). To reduce variability, 15 samples from each of the four groups were built simultaneously on the same plate to control process consistency. Figure 2 represents the build layout for fabrication of specimens. This approach helps to control any minor process variations that might occur during the build.

2.3 Post-processing

To evaluate the impact of chemical and electrochemical surface treatments on fatigue performance, four sets of specimens were tested. One group remained in the as-built condition as a baseline, while the other three underwent different post-processing treatments, detailed in Table 3.

The Hirtisation® process involves three main steps, shown in Fig. 3: (1) removal of sintered particles and supports using Hirtisation® SS-Auxilex Pro electrolyte, (2)

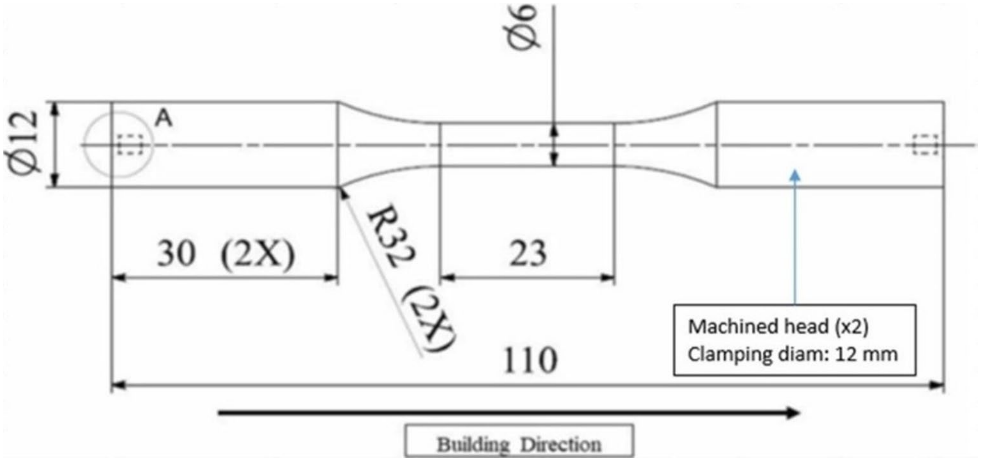

Fig. 1 Specimen geometry for high cycle fatigue tests

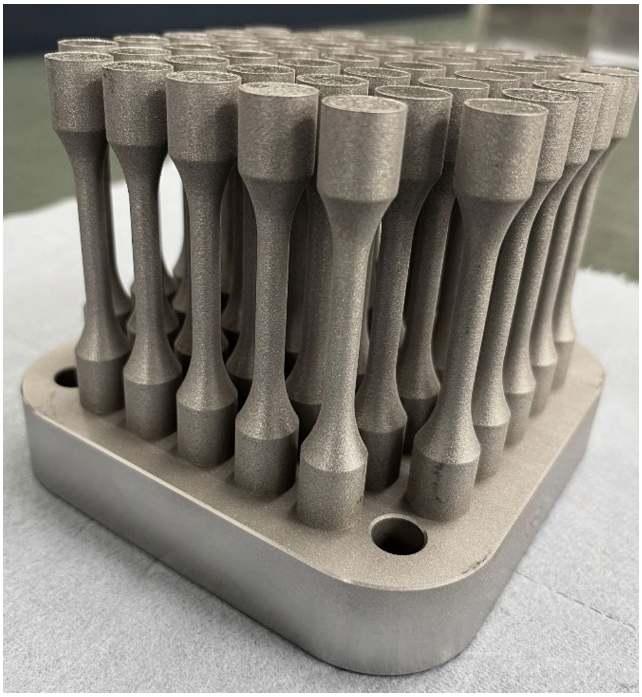

Fig. 2 Samples on the build plate

Table 3 Details of the sample classification

Sample group	Condition	Number of samples
U	As-built condition	15
A	Hirtisation® (using only step 1 for a long time)	15
B	Hirtisation® (using step 1 and step 3)	15
B+D	Hirtisation® followed by DLyte	15

surface conditioning and cleaning with ES-Delevatex eco electrolyte, and (3) optional surface polishing using ES-Politurex electrolyte if further smoothening is needed for the application.

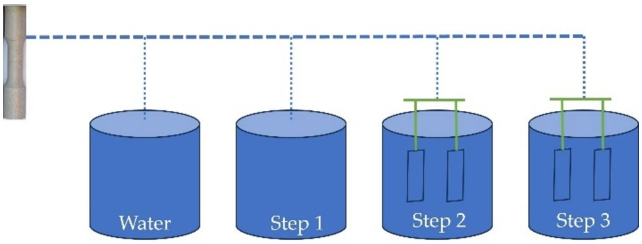

Fig. 3 Schematic of the Hirtisation® process for 316L stainless steel

Table 4 Parameters for B samples

Step	Time, min	Temperature, °C	Nature of the bath
Step 1	50–75	65–80	Chemical
Step 3	50–75	65–85	Electrochemical

Hirtisation® was conducted using the H3000 automated finishing system from RENA Technologies, Austria. Key process parameters include power level, which is linked to the surface area of the component, electrical current, bath temperature, and treatment time.

Sample set A underwent a one-step treatment in bath 1 for approximately 365 min, followed by rinsing with distilled water and vacuum drying at 50 °C for 20 min. Due to the extended exposure, higher material loss is expected. The duration of treatment was selected based on manufacturer recommendations and iterative trials.

Sample set B received a two-step Fe alloy treatment using baths 1 and 3. Parameters are listed in Table 4. Step 1 was non-electrical, while step 3 used 100% power. After each step, samples were rinsed and vacuum dried at 50 °C for 20 min. Step 2 was initially evaluated during process optimisation, however, for sample set B, no significant further improvement in surface quality was achieved beyond the combination of Steps 1 and 3. Therefore, only Steps 1 and 3 were applied to the fatigue samples.

The parameter "100% power" in Hirtisation refers to the fixed operating setting defined by the equipment manufacturer for the applied current density. This is not a variable parameter adjusted by the user but rather the standard operational setting.

Samples from the B + D set underwent treatment B, followed by additional processing using the DLyte system from GPA Innova (Barcelona, Spain) to further reduce surface roughness. During DLyte treatment, samples were mounted on a holder and rotated in a solid electrolyte while an electric current was applied. A polishing time of 3 h was employed, using an electrolyte formulated specifically for iron-based alloys. A proprietary electrolyte formulation designed specifically for stainless steels was used during DLyte processing. Specimen mass was measured before and after each post-processing step using a calibrated analytical balance (Mettler Toledo XS205DU, readability 0.01 mg). Each mass value represents the mean of three repeated measurements.

2.4 Characterization

2.4.1 Surface roughness

Surface roughness was measured using a Sensofar S neox confocal microscope (20x, 1.29 µm resolution) with stitched 3 × 3 scans. MountainsMap software (ISO 25178-2:2012) calculated Sa and S10z from multiple gauge locations on two samples per group to evaluate surface texture's effect on fatigue [15].

2.4.2 Residual stress

Residual stresses were measured via XRD (Stresstech G2R XStress 3000, Mn Kα, λ = 0.21031 nm) using the modified $\sin^2\psi$ method and Hooke's Law (E = 199.9 GPa, ν = 0.29) 16. Measurements targeted fatigue specimen gauge lengths with depth profiling by electro-polishing. Tests complied with SS-EN 15305:2008 in an accredited lab [16].

2.4.3 Fatigue testing

Fatigue testing followed ISO 1099:2017 with pulsating stress (R = 0.1) at 10 Hz using stress amplitudes of 247.5, 202.5, and 157.5 MPa. Five specimens per level were tested at room temperature. Fatigue data for the as-built (U) condition at 202.5 MPa are not included, as several specimens failed prematurely during alignment, leaving too few valid tests for statistical evaluation. Nominal stress was based on measured cross-sections. Fracture surfaces were examined via stereomicroscope and LEO Gemini 450 Field Emission Gun Scanning Electron Microscope (FEGSEM) for high-resolution imaging.

2.4.4 Microstructure

Microstructural analysis was conducted on cross-sections from the gauge section, prepared perpendicular to the surface. Samples were hot-mounted, ground with SiC paper, and polished to a mirror finish for electron backscatter diffraction (EBSD). EBSD, used for crystallographic texture and grain size analysis, was performed with an Oxford Instruments Nordlys II system. Data analysis utilized MTEX, an open-source MATLAB toolbox for texture analysis.

3 Results

3.1 Dimensional evaluation

As-built (U) specimens were the baseline for dimensional comparison, with at least 5 measurements per sample. Radial reductions were ~ 0.32 mm (A), 0.16 mm (B), and 0.21 mm (B + D) (Fig. 4a). Mass loss (Fig. 4b) was ~ 9% (A), 5% (B), and 6% (B + D), consistent with dimensional changes, with A showing the greatest material removal.

3.2 Surface characterisation

Figure 5 shows top-view microscopy images of samples (U, A, B, B + D), revealing clear distinctions in surface morphology due to post-processing. Visual observations confirm roughness measurements.

Confocal microscopy (Fig. 6) quantitatively corroborates improved surface quality, presenting key roughness parameters (Sa, S5v, S10z, Sdq) for all sample groups (U, A, B, B + D) based on five measurements per sample. These data, combined with Fig. 5's visual observations, offer in-depth understanding of post-processing effects on surface properties and fatigue behaviour.

Figure 6a shows the average surface roughness (Sa), revealing a significant reduction from the as-built (U) condition (11 µm) across all post-processed groups. Sample A achieved an over 80% reduction to 1.7 µm, while B saw over a 60% decrease to 4 µm. The smoothest surface was achieved with the B + D combination, yielding an Sa of 1.5 µm (over 85% reduction). Similar trends were observed for S5v (Fig. 6b), decreasing from 28 µm (U) to 17 µm (A), 24 µm (B), and 7.1 µm (B + D). S10z (Fig. 6c) also followed this pattern, dropping from 82 µm (U) to 27 µm (A), 43 µm (B), and 11 µm (B + D). Finally, Sdq (Fig. 6d), representing overall surface variation, significantly decreased from 1.8 µm (U) to 0.26 µm (A), 0.3 µm (B), and a lowest value of 0.03 µm (B + D).

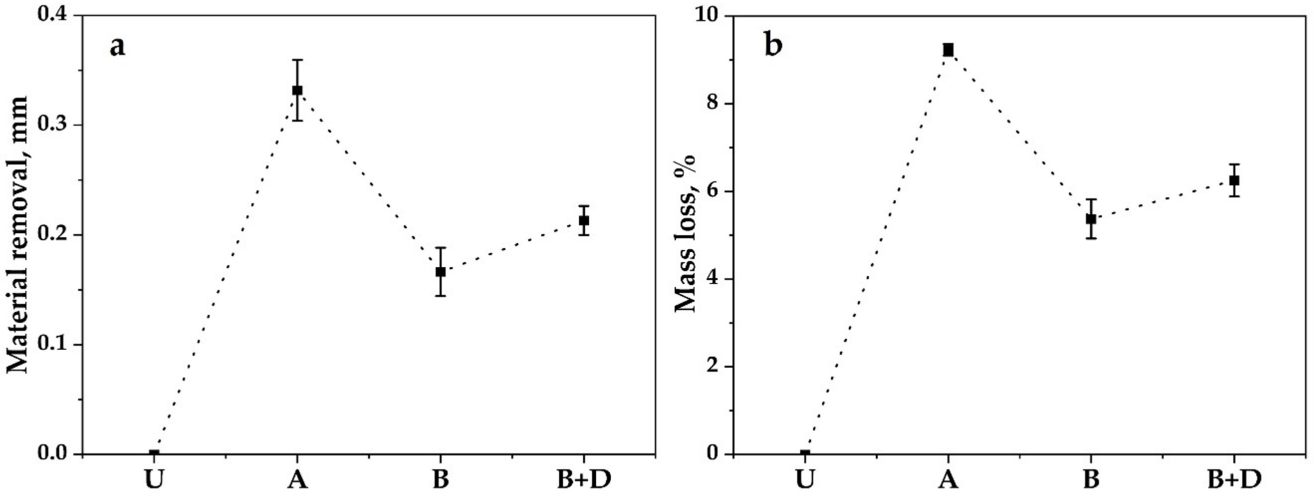

Fig. 4 Plot depicting **a** material removal, **b** radial dimensional change for different post-processing conditions

Fig. 5 Qualitative observation of the fatigue samples in the top view illustrating the observable difference in surface quality

3.3 Residual stresses-X-ray diffraction

Figure 7 presents individual residual stress (RS) depth profiles for all conditions (U, A, B, B+D). To ensure accurate comparison despite surface variations from post-processing, a geometrically equivalent depth was chosen. For U specimens, surface RS was ~400 MPa, decreasing slightly to ~385 MPa at 20 µm. A peak of ~600 MPa was observed at 35 µm, after which RS stabilized between 500–550 MPa deeper within the material. In contrast to as-built specimens (~400 MPa), all post-processed surfaces (A, B, B+D) showed higher tensile residual stresses, averaging ~635 MPa. A notable "hook-shaped" residual stress profile characterized these treated specimens: stress initially decreased to ~450 MPa at 7 µm (similar to U specimens), but then rose again beyond 7 µm, defining the observed profiles for A, B, and B+D. The post-processing treatments do not induce or relieve residual stresses in the bulk material. The small variations observed beyond ~0.3 mm result from stress redistribution and the altered surface reference following material removal.

3.4 Microstructure characterisation

Figure 8 presents SEM images of fatigue bars (U, A, B, B+D), illustrating surface changes from post-processing. The as-built (U) sample (8a, 8b) shows semi-sintered particles typical of the process, which are largely removed after post-processing (8c–h). Treatment A (8c, 8d) shows coral-like surfaces devoid of semi-sintered particles, exposing melt pools. Sample B (8e, 8f) reveals craters from dislodged particles during Hirtisation®. Electrochemical treatment (B) exposed grain boundaries and cellular structures. DLyte post-Hirtisation® (B+D) significantly altered surface morphology, masking features like melt pool and grain boundaries seen in earlier conditions.

Figure 9 shows the as-built (U) specimen's microstructure in both xy- and z-directions. Fine contour grains near the edge (Fig. 9a and b) result from rapid solidification, while coarser grains form in the core due to slower cooling. Epitaxial growth is evident along the z-axis (Fig. 9d). EBSD (Fig. 10) confirms this edge-to-core grain coarsening.

Figure 11 links microstructure (SEM) and surface roughness, focusing on the edge microstructure of post-processed specimens (A, B, B+D). A key commonality is the absence of a distinct "contour" region (Fig. 9), indicating effective removal by all post-processing. The B+D specimen shows a well-defined surface curvature (Fig. 11e, f), unlike the less defined borders of A and B (Figs. 11a and 12d). This superior B+D curvature correlates with its lowest average surface roughness, suggesting a link between post-processing-influenced edge morphology and overall surface roughness.

3.5 Fatigue testing

Figure 12 presents the average fatigue life and data spread for each surface condition (U, A, B, B+D) and stress amplitude.

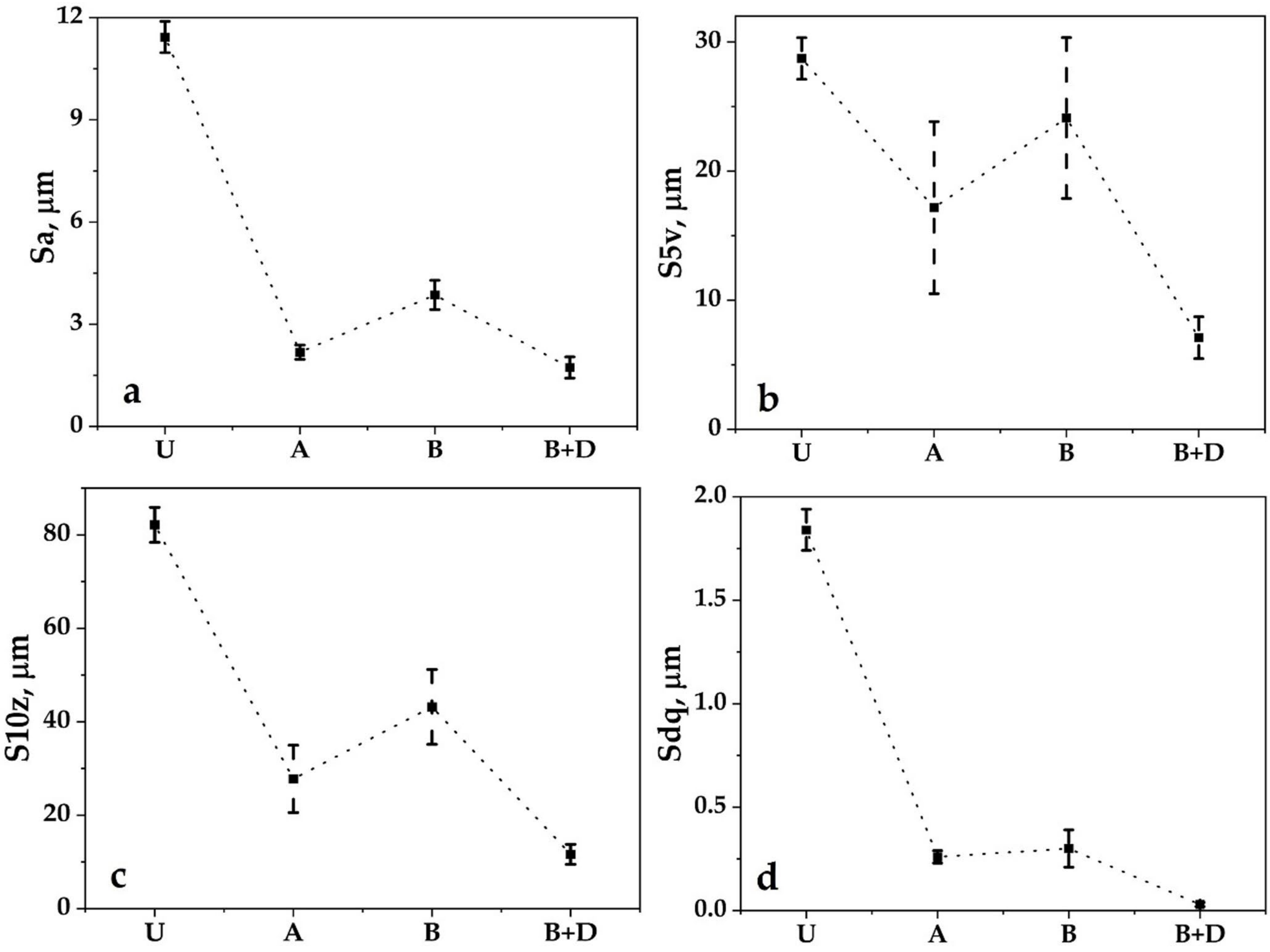

Fig. 6 Roughness **a** S_a, **b** S_{5v}, **c** S_{10z} and **d** S_{dq} measured by confocal microscopy

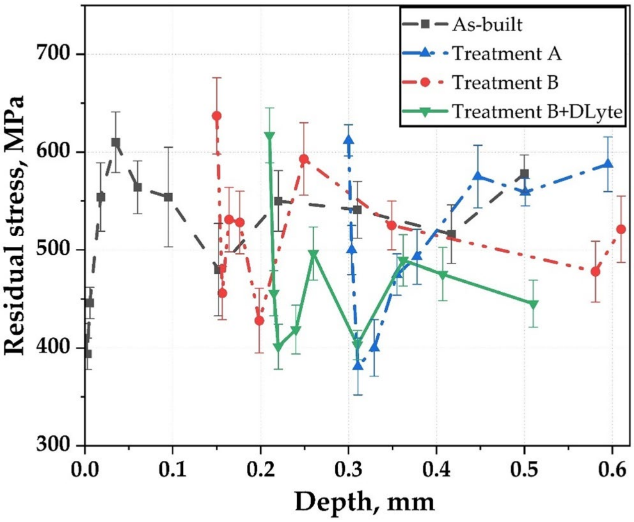

Fig. 7 Residual stress depth profile for different conditions under study

All post-processed conditions showed slight improvement in average fatigue life compared to the as-built state, particularly at higher stress amplitudes (247.5 MPa). Here, A and B treatments showed similar improvements (approx. 22–24%), while B + D specimens displayed the most significant enhancement (40% increase). At the intermediate stress (202.5 MPa), despite limited as-built data for direct comparison, B and B + D improved by 12% and 17%, respectively, while A showed the lowest average fatigue life among post-processed conditions. At the lowest stress (157.5 MPa), B exhibited substantial improvement (40%), A showed marginal improvement (4%), and B + D had the most significant enhancement at this level. Notably, the largest scattering was observed in B + D specimens at 157.5 MPa. However, a consistent observation across all tested specimens is that the post-processed specimens performed similar to the as-built specimens.

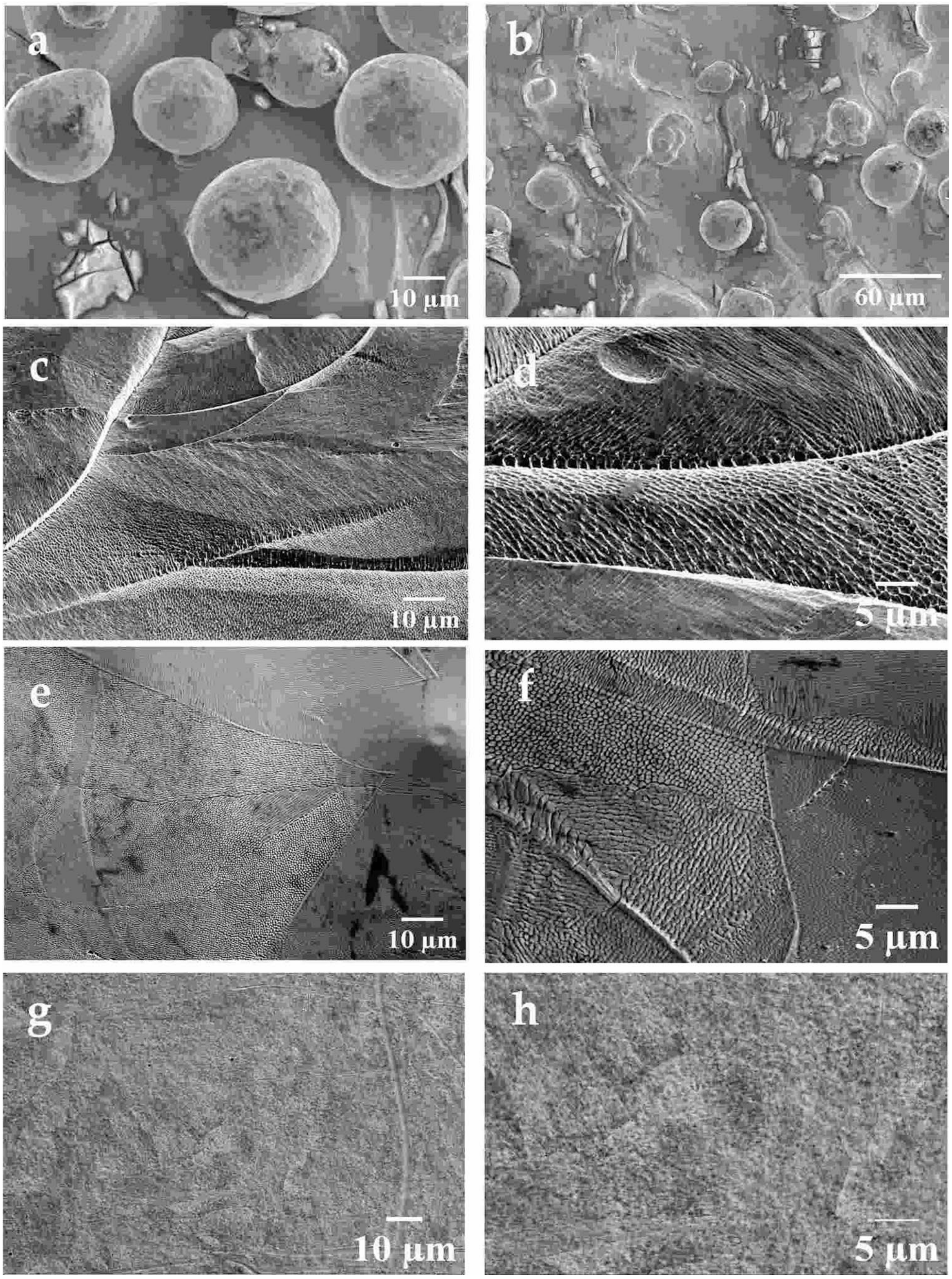

Fig. 8 Surface features of specimens in different conditions **a** and **b** U, **c** and **d** A, **e** and **f** B, and **g** and **h** B+D

3.6 Fractography

Fatigue failure has three stages: crack initiation, crack growth (fatigue zone), and fracture (overload zone) [17, 18]. Figure 13 stereo micrographs show these zones, with fatigue zone size varying by surface condition and stress. *Fractography revealed that as-built specimens exhibited multiple crack initiation sites due to surface irregularities and unfused particles, while Hirtisation®-treated specimens showed predominantly single initiation sites.* Post-Hirtisation® samples had larger fatigue zones than as-built at the same stress (Fig. 13a and b). Higher stresses increased fracture zones, indicating slower crack growth at lower stress. SEM (Fig. 14a) showed mainly transgranular crack growth with striations, while the overload zone exhibited ductile, dimpled failure (Fig. 14b), revealing fatigue and failure behavior.

Figure 15a and b show multiple crack initiation points near the surface on as-built specimens, linked to process defects. Treatment A specimens (Fig. 15c and d) exhibit a coral reef-like etching pattern at crack sites. For both A and B specimens, crack initiation is mainly associated with Hirtisation-induced features like etching and craters. Figure 15e and f highlight craters acting as stress concentrators

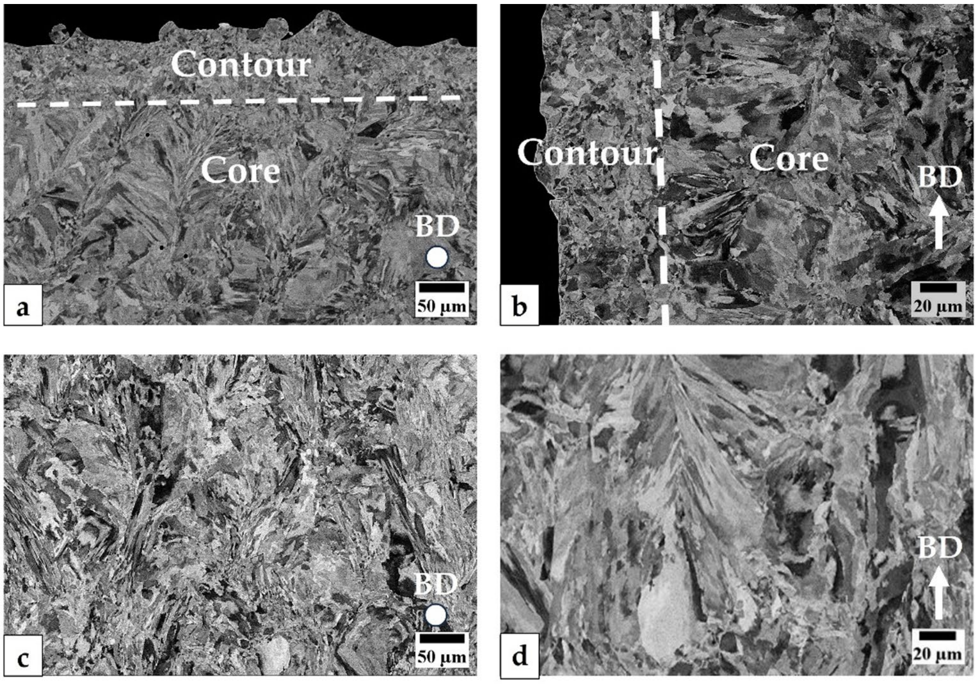

Fig. 9 Cross-section of U specimen in different directions **a** and **c** perpendicular, and **b** and **d** in the building direction

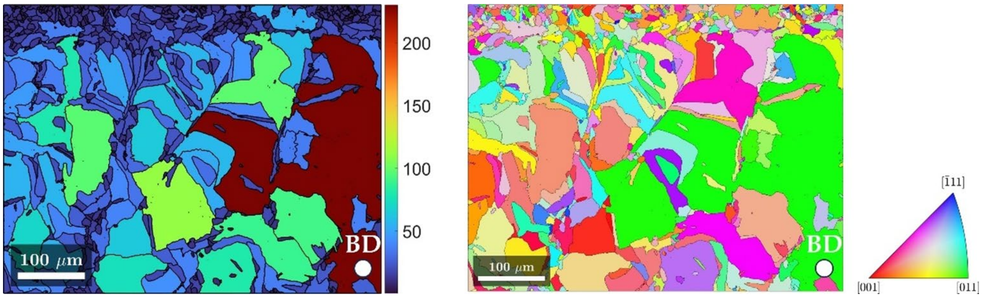

Fig. 10 EBSD maps showing grain size distribution and orientation close to the edge of the U specimen in XY plane

in B specimens. Figure 15g and h suggest B + D specimens' crack initiation involves both pre-existing defects and processing-induced features.

4 Discussions

4.1 Effect of Hirtisation® on dimensional tolerance and surface roughness

The dimensional analysis highlights a clear trade-off between material removal and surface quality across the post-processing treatments. Specimens from treatment A experienced the highest material removal due to extended chemical bath exposure during Hirtisation®, which effectively removes support structures and smooths the surface but at the cost of significant dimensional reduction. In contrast, treatment B, with a shorter chemical step followed by a milder electrochemical polishing, reduced material removal while still improving surface roughness substantially. The combined B + D treatment demonstrated the best balance, achieving the lowest material removal alongside superior surface finish, indicating its potential for applications where dimensional tolerances are critical. These findings emphasize the importance of integrating post-processing effects into the Design for Additive Manufacturing (DfAM) workflow, particularly for components with tight dimensional requirements. The correlation between material removal and radial dimension reduction underlines the necessity of accounting for these changes during the design phase to ensure final part accuracy.

Surface topography analysis further elucidates the mechanisms behind fatigue behaviour (Fig. 16). The crater-like features observed in B specimens are most likely associated with the exposure of pre-existing subsurface imperfections located at the contour–hatch interface. The measured material removal supports this interpretation: the contour layer appears fully removed in series A but only partially exposed in series B and B + D, where the surface coincides with the contour–hatch transition zone, a region known to contain internal porosity and unfused defects. Melt-pool boundaries remain visible in A specimens, while the B + D treatment

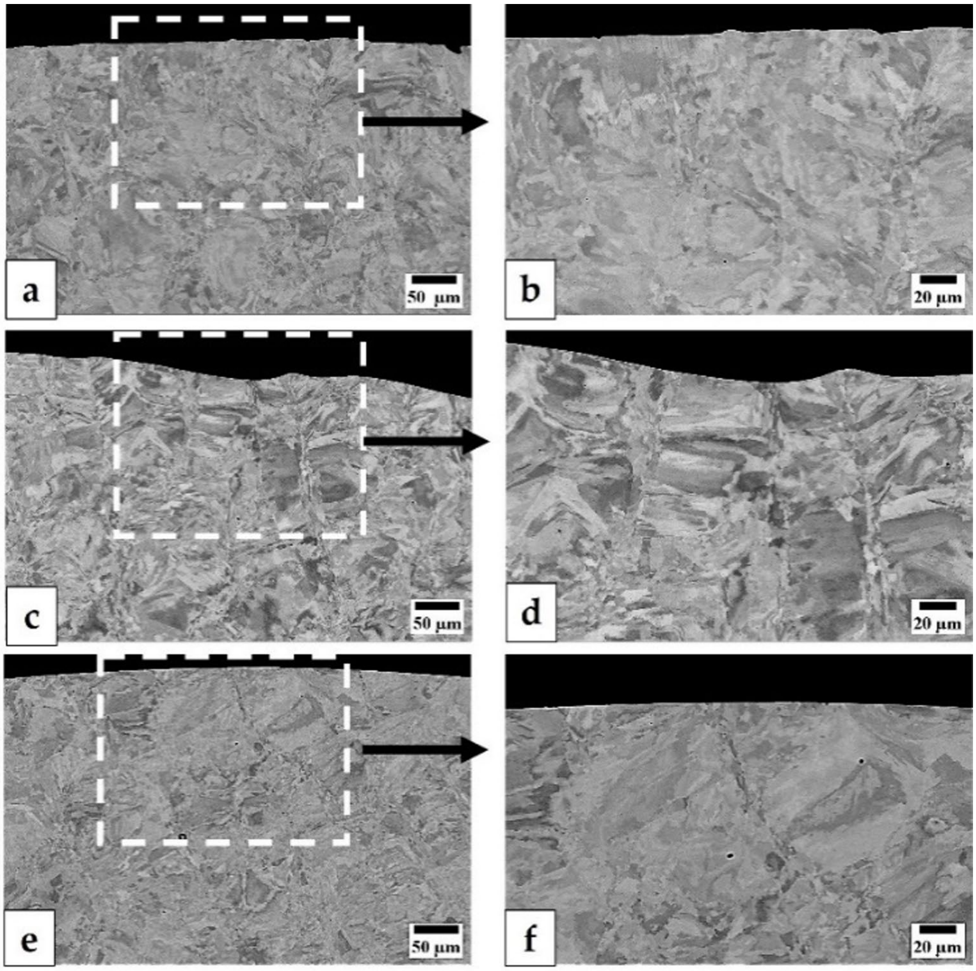

Fig. 11 Cross-section of specimens in different post-processing conditions **a** and **b** specimen set A, **c** and **d** specimen set B, and **e** and **f** specimen set B + D

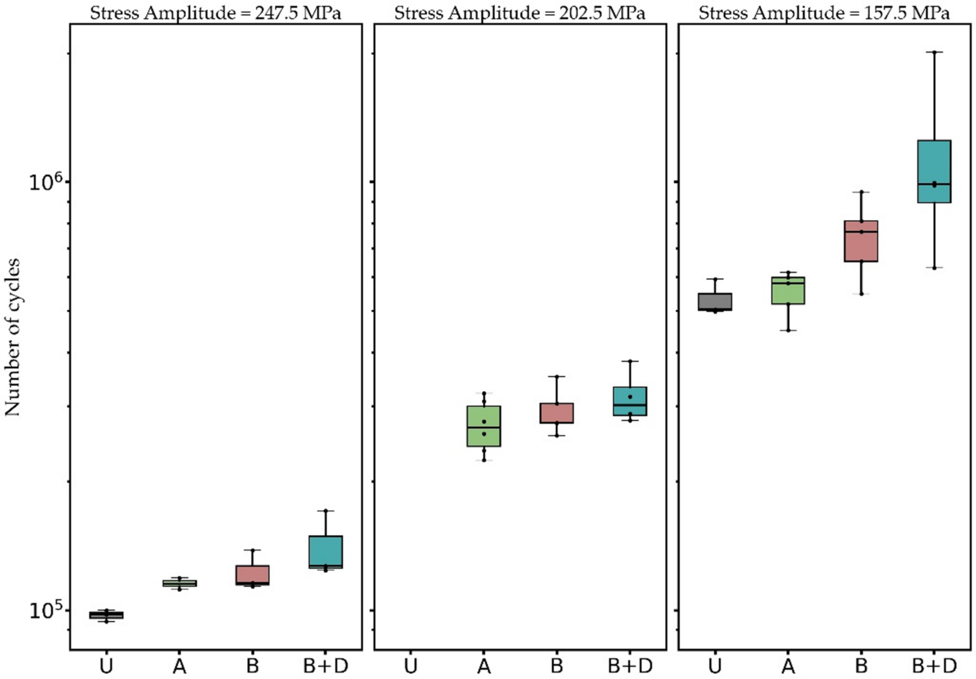

Fig. 12 Fatigue life of each specimen condition at different stress amplitudes. The rectangular boxes represent the range of measured fatigue lives, with the horizontal line inside each box indicating the mean fatigue life (average number of cycles to failure). *Note* Data for the as-built (U) condition at 202.5 MPa are not shown due to premature specimen failure during alignment

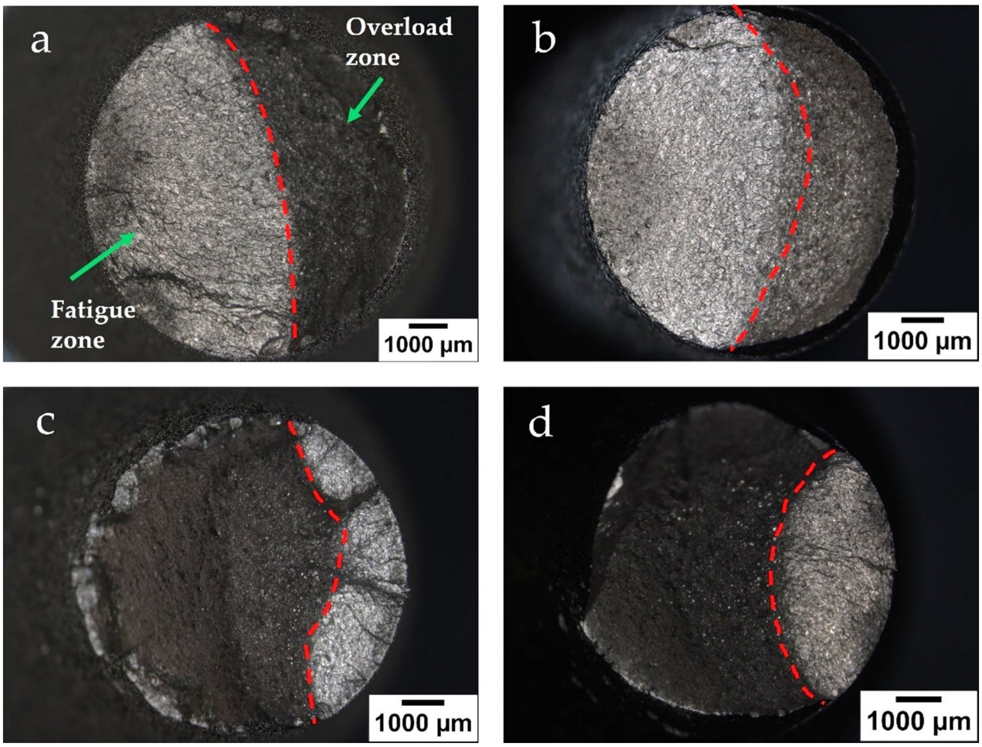

Fig. 13 Stereo micrographs showing the two distinct regions of the fracture surface, crack growth (fatigue zone) and fracture (overloaded zone) of as-built condition specimens tested at **a** 157.5 and **c** 247.5 MPa, respectively and in post-Hirtisation® condition, treatment A, specimens at **b** 157.5 and **d** 247.5 MPa, respectively

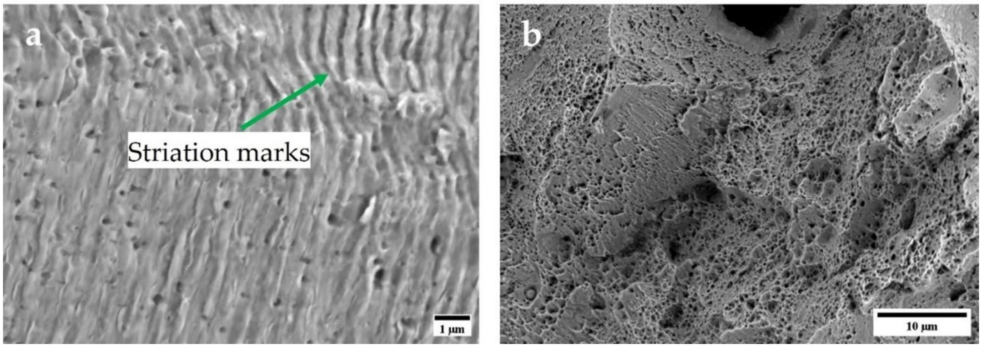

Fig. 14 SEM micrographs showing the two distinct zones of fatigue fracture surfaces **a** Striation marks in the fatigue zone, **b** dimpled features in the overload zone

yields a markedly smoother surface devoid of these stress concentrators. This smoother surface aligns with improved fatigue resistance by minimizing potential crack initiation sites.

Overall, the combination of chemical and electrochemical processes with DLyte polishing offers an optimized approach to enhance surface quality while controlling material removal, which is crucial for maintaining dimensional integrity and improving fatigue performance in PBF-LB/M 316L stainless steel components.

4.2 Fatigue behaviour

Understanding fatigue in AM 316L SS requires analyzing cellular solidification morphology (Fig. 17). Treatment A's chemical etching creates a coral reef-like structure (Fig. 17a) from prolonged Hirtisation® Step 1. Treatment B's electrochemical step reveals cell boundaries without coral reef features (Fig. 17b), linking these features to extended Hirtisation®.

Beyond surface features, residual stress plays a critical role in the fatigue behavior of additively manufactured (AM) 316L stainless steel. AM processes like PBF-LB/M induce significant internal stresses during fabrication due to thermal gradients. These stresses can cause immediate cracking or remain "frozen" within the component, leading to premature failure under operational loads [19]. Therefore, comprehensive characterization of residual stress distribution in as-built structures is vital for manufacturing success and part longevity. The unique columnar grain structure and crystallographic texture typical of AM also influence residual stress development [20]. Post-processing (e.g., heat treatment) may be necessary to mitigate these stresses if not addressed during design [19].

Fig. 15 Fractography of different specimen conditions, **a** and **b** U, **c** and **d** A, **e** and **f** B, and **g** and **h** B+D

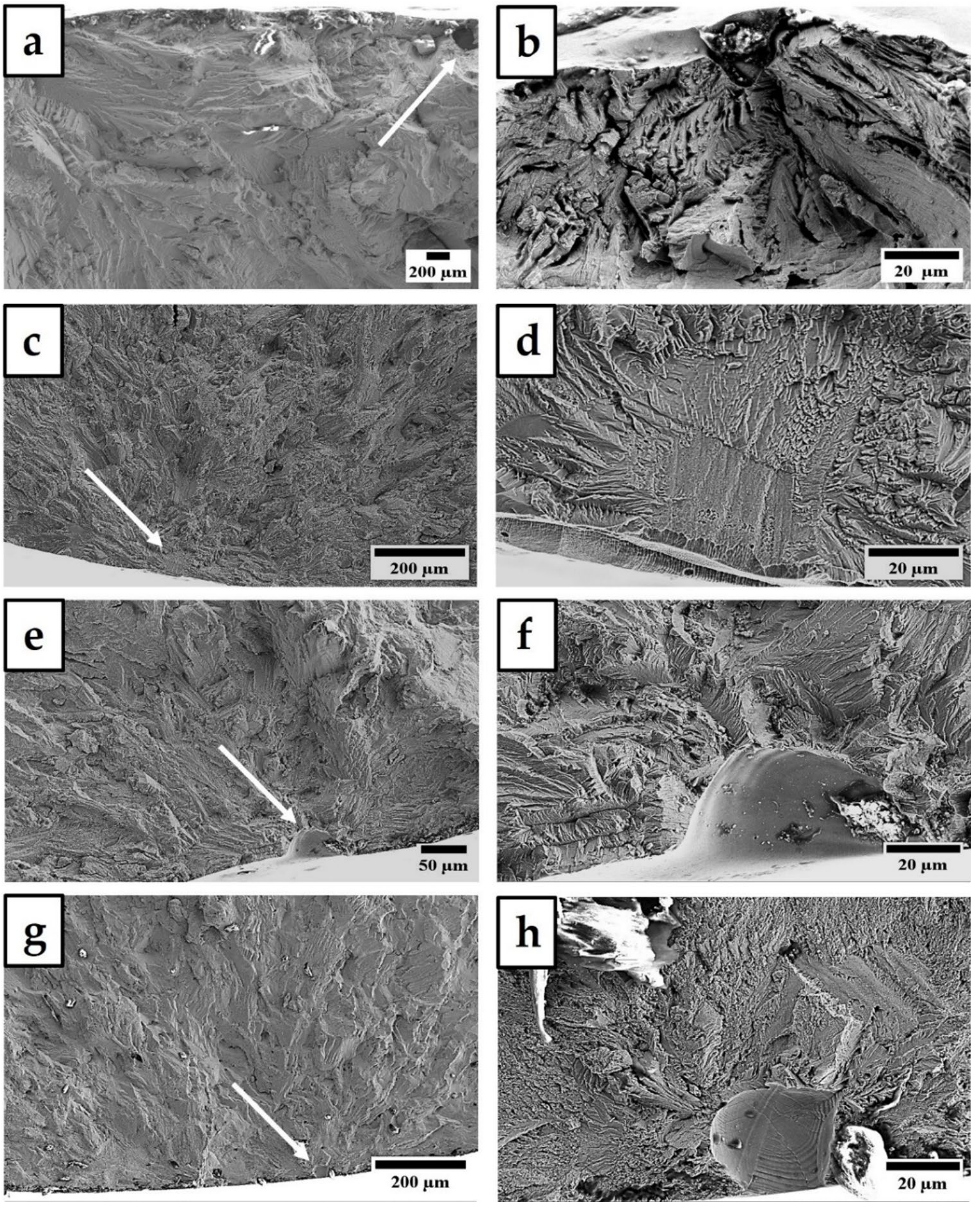

Existing research extensively covers residual stress in PBF-LB/M 316L [21]. Simson et al. [22] used X-ray diffraction, finding higher residual stress along the scan direction at the top surface, perpendicular to the scan direction at the lateral surface. This aligns with temperature gradient and cool-down mechanisms of stress generation [23]. Stress values also depended on structural density and adherence of unfused powder. While high tensile stresses at the surface, detrimental to fatigue, decrease inwards [24], a limitation of current studies is the lack of deeper residual stress data. A complete picture, capturing the tensile-to-compressive transition, is needed for a comprehensive understanding of stress distribution and its impact on fatigue.

The scatter in fatigue data for post-processed specimens (Fig. 13) is consistent with prior research [25], often linked to the size and location of internal defects. A review by Avanzini et al. [26] on PBF-LB/M 316L fatigue under various surface conditions (excluding heat treatment) found that machined samples (Ra 0.05–1.8 µm) showed run-out at 10^7 cycles between 140 and 220 MPa [27–29], and polished samples between 120 and 190 MPa [30, 31]. Our study's samples did not achieve run-out at these stress levels, indicating inferior fatigue performance. Significant data scatter persists even in machined/polished samples, likely due to the inherent process-dependent nature of AM properties and varying processing parameters/sample extraction methods. Techniques like shot peening can enhance fatigue performance, especially in stress-relieved materials, by inducing near-surface compressive residual stresses comparable to machined surfaces [32]. However, in materials with high

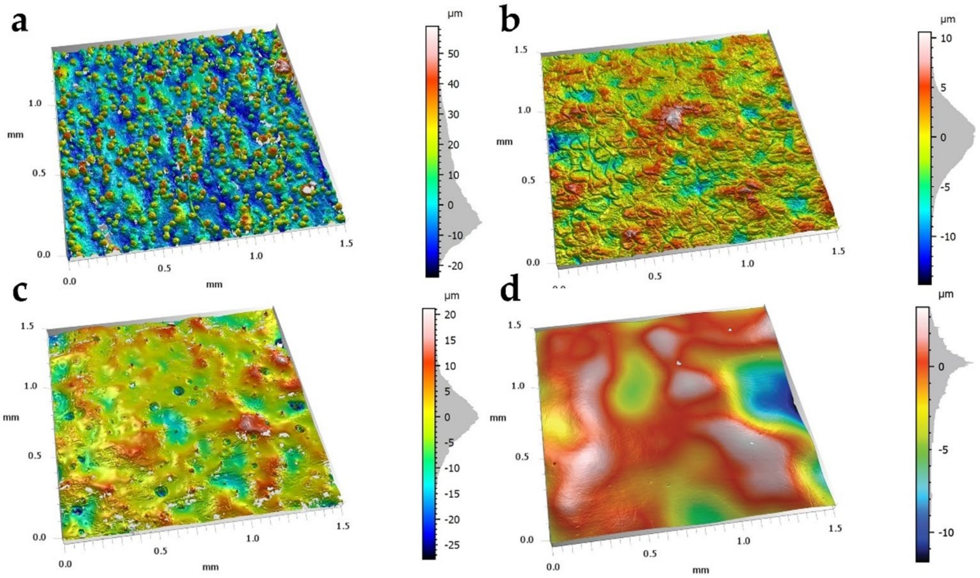

Fig. 16 Surface 3D plots of specimens in different conditions, **a** U, **b** A, **c** B, and **d** B + D

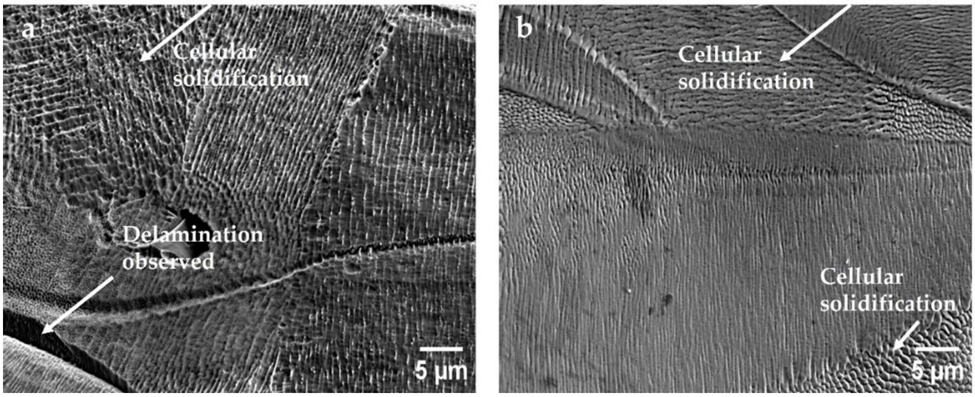

Fig. 17 Surface features of specimen set **a** A, and **b** B

pre-existing tensile residual stresses, as in the present study, the overall effect of shot peening is more complex and may not yield comparable improvements to those observed in stress-relieved or machined conditions.

In the present study, in spite of the excellent surface topography, the inferior fatigue performance of the B + D specimens is attributed to the tensile residual stresses present at the surface after post-processing. The chemical and electrochemical post-processing techniques used here, lacking a mechanical component, negligibly affect the overall stress state. However, material removal triggers a redistribution of stresses, leading to observed increases in surface residual stress. Combining surface characterization, residual stress assessment, and fractographic analysis can provide a deeper understanding of their interaction and influence on fatigue.

The specimens in this study were intentionally not heat-treated prior to surface finishing, which contributed to the relatively high tensile residual stresses measured at the surface (Fig. 7). Previous studies on PBF-LB/M 316L stainless steel have shown that stress-relief heat treatments significantly reduce near-surface tensile residual stresses and may also modify the material's texture and dislocation substructure [33]. In the present dataset, the combined B + D condition exhibited the lowest Sa value yet only a limited improvement in fatigue performance, indicating that tensile residual stresses counteracted the beneficial effect of reduced surface roughness. It can therefore be inferred that applying a stress-relief treatment before chemical or electrochemical finishing would further enhance fatigue resistance, particularly for the B + D condition, by lowering the driving force for early crack initiation and allowing the improved surface morphology to dominate the fatigue response. Although heat treatment may induce some microstructural coarsening, its influence is expected to be secondary in the high-cycle regime considered here. However, potential dimensional changes should be accounted for during design DfAM. Overall, these findings support a process route in which stress relief precedes surface finishing to maximize fatigue performance in PBF-LB/M 316L stainless steel.

Fractographic analysis revealed spherical pores with distinct concentric ridges on fracture surfaces of U and B + D specimens (Fig. 18). These are pre-existing defects,

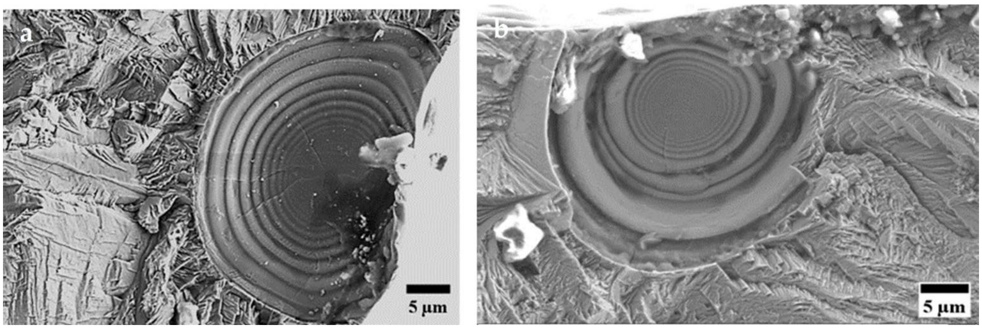

Fig. 18 Fracture surface showing the concentric ridges in **a** U, and **b** B + D specimen

not fatigue-induced, and differ from lack-of-fusion or gas entrapment defects [34]. Their formation mechanism is linked to the laser scanning process, specifically incomplete re-melting of localized surface areas from previous layers, which impedes molten material spread. This phenomenon involves a triple line (gas–solid-liquid contact point), vertical surface tension force, and substrate deformation due to atomic diffusion at elevated processing temperatures [34].

Fractographic analysis of specimens B identifies craters as key factors reducing fatigue life. These craters act as severe stress concentrators, elevating local stress intensity factors (K_t) and promoting crack initiation and propagation under cyclic loading [35]. Combined with high surface tensile stresses, craters significantly lower fatigue performance. In specimen set A, chemical post-processing preserves melt pool patterns, revealing valleys and delamination-like features between melt pools. These defects, visible up to 20 µm into the fracture (Fig. 15f), also serve as fatigue crack initiation sites, contributing to the lowest fatigue life among the three groups. By integrating surface feature analysis, residual stress measurement, and fractography, this study enhances understanding of fatigue behavior in AM components, supporting improved post-processing methods for better fatigue resistance.

5 Conclusions

This study examined how surface modification and residual stresses interact to determine the fatigue performance of PBF-LB/M 316L stainless steel. The findings highlight the importance of balancing surface refinement with stress management in additive manufacturing.

The key conclusions of this study can be summarized as follows:

- Hirtisation® effectively improved surface quality, reducing average roughness by approximately 70–80% through the removal of semi-fused particles and contour irregularities.
- The combined Hirtisation® + DLyte treatment achieved the smoothest surface (Sa ≈ 1.5 µm) and the most uniform topography, confirming the complementary nature of chemical and electrochemical finishing.
- Fatigue life increased by up to 40% for the combined treatment compared with the as-built condition, demonstrating that surface refinement delays fatigue crack initiation.
- High tensile residual stresses (> 500 MPa) remained after post-processing, counteracting the benefits of smoother surfaces and explaining the limited overall fatigue improvement of post-processed specimens.
- Fatigue behaviour is governed by the interaction between residual stress and surface morphology, rather than by surface roughness alone.
- Applying stress-relief heat treatment before surface finishing is expected to further enhance fatigue resistance by reducing tensile residual stresses and enabling surface quality to dominate the fatigue response.
- Design for Additive Manufacturing (DfAM) should incorporate expected material removal, dimensional changes, and stress-relief steps during design and post-processing planning to ensure both geometric accuracy and optimal fatigue performance.

Acknowledgements This work was carried out within the framework of the Centre for Additive Manufacturing—Metal (CAM2), supported by the Swedish Governmental Agency for Innovation Systems (Vinnova 2022-03076). The authors also gratefully acknowledge the funding provided by Västra Götland Region in the form of project COMPASS II (MRU 2023-00440) at the Research Institutes of Sweden (RISE) AB. Additionally, the authors extend their appreciation to the Application Centre for Additive Manufacturing at RISE AB. The authors would like to thank Dr. Bala Malladi for his help with EBSD analysis. Finally, the authors would like to express their sincere gratitude to Dr Jonas Holmberg and Dr. Johan Berglund for their assistance with the X-ray diffraction and surface roughness measurements.

Author contributions SM wrote the manuscript text while all the other authors edited the manuscript. FP, ED, and MH contributed through processing and testing of the specimens. UK is responsible for project management. SH is responsible for funding acquisition and supervision.

Funding Open access funding provided by RISE Research Institutes

of Sweden.

Data availability No datasets were generated or analysed during the current study.

Declarations

Conflict of interest The authors declare no competing interests.

References

1. DebRoy T et al (2018) Additive manufacturing of metallic components – process, structure and properties. Prog Mater Sci 92:112–224
2. Beevers E et al (2024) Effect of Hirtisation treatment on surface quality and mechanical properties of AlSi10Mg samples produced by laser powder bed fusion. Mater Today Commun 38:108042
3. Chern AH et al (2019) A review on the fatigue behavior of Ti-6Al-4V fabricated by electron beam melting additive manufacturing. Int J Fatigue 119:173–184
4. Hamidi M, et al (2017) Finishing of internal and external surfaces produced by Powder Bed Fusion. https://www.euspen.eu
5. Prochaska S, Hildreth O (2022) Effect of chemically accelerated vibratory finishing on the corrosion behavior of laser powder bed fusion 316L stainless steel. J Mater Process Technol. https://doi.org/10.1016/j.jmatprotec.2022.117596
6. Sadeghi M, Diaz A, McFadden P, Sadeghi E (2022) Chemical and mechanical post-processing of Alloy 718 built via electron beam-powder bed fusion: surface texture and corrosion behavior. Mater Des 214:110405
7. Maleki E, Bagherifard S, Bandini M, Guagliano M (2021) Surface post-treatments for metal additive manufacturing: progress, challenges, and opportunities. Addit Manuf 37:101619
8. Pourrahimi S, Hof LA (2024) On the post-processing of complex additive manufactured metallic parts: a review. Adv Eng Mater. https://doi.org/10.1002/adem.202301511
9. Jain S, Corliss M, Tai B, Hung WN (2019) Electrochemical polishing of selective laser melted Inconel 718. Procedia Manuf 34:239–246
10. Oosterbeek RN, Sirbu G, Hansal S, Nai K, Jeffers JRT (2023) Effect of chemical–electrochemical surface treatment on the roughness and fatigue performance of porous titanium lattice structures. Addit Manuf 78:103896
11. Sandell V, Nilsson J, Hansson T, Åkerfeldt P, Antti M-L (2022) Effect of chemical post-processing on surfaces and sub-surface defects in electron beam melted Ti-6Al-4V. Mater Charact 193:112281
12. Taljaard DJ, Fourie J, Kloppers CP (2023) The effect of sandblasting and bead blasting on the surface finish of dry electrolyte polishing of laser powder bed fusion parts. J Mater Eng Perform 32:2050–2061
13. Rautio T, Jaskari M, Järvenpää A (2023) Surface roughness improvement of PBF-LB manufactured 316L with dry electropolishing. Key Eng Mater 972:3–12
14. Hatami S, Ma T, Vuoristo T, Bertilsson J, Lyckfeldt O (2020) Fatigue strength of 316 L stainless steel manufactured by selective laser melting. J Mater Eng Perform 29:3183–3194
15. Flys O, Berglund J, Rosen B-G (2020) Using confocal fusion for measurement of metal AM surface texture. Surf Topogr Metrol Prop 8:24003
16. Salmi A, Atzeni E (2017) History of residual stresses during the production phases of AlSi10Mg parts processed by powder bed additive manufacturing technology. Virtual Phys Prototyp 12:153–160
17. Sachs NW (2005) Understanding the surface features of fatigue fractures: how they describe the failure cause and the failure history. J Fail Anal Prev 5:11–15
18. Djoković JM, Nikolić RR, Bujnák J, Hadzima B (2018) Estimate of the steel bridges fatigue life by application of the fracture mechanics. IOP Conf Ser Mater Sci Eng 419:012010
19. Fang Z-C, Wu Z-L, Huang C-G, Wu C-W (2020) Review on residual stress in selective laser melting additive manufacturing of alloy parts. Opt Laser Technol 129:106283
20. Chao Q et al (2021) The effect of post-processing heat treatment on the microstructure, residual stress and mechanical properties of selective laser melted 316L stainless steel. Mater Sci Eng A 821:141611
21. Behjat A, Lannunziata E, Gadalińska E, Iuliano L, Saboori A (2023) Improving the surface quality and mechanical properties of additively manufactured AISI 316L stainless steel by different surface post-treatment. Procedia CIRP 118:771–776
22. Simson T, Emmel A, Dwars A, Böhm J (2017) Residual stress measurements on AISI 316L samples manufactured by selective laser melting. Addit Manuf 17:183–189
23. Mercelis P, Kruth J (2006) Residual stresses in selective laser sintering and selective laser melting. Rapid Prototyp J 12:254–265
24. Wu AS, Brown DW, Kumar M, Gallegos GF, King WE (2014) An experimental investigation into additive manufacturing-induced residual stresses in 316L stainless steel. Metall Mater Trans A 45:6260–6270
25. Shrestha R, Simsiriwong J, Shamsaei N (2019) Fatigue behavior of additive manufactured 316L stainless steel parts: effects of layer orientation and surface roughness. Addit Manuf 28:23–38
26. Avanzini A (2023) Fatigue behavior of additively manufactured stainless steel 316L. Materials 16:65
27. Voloskov B et al (2020) Very high cycle fatigue behavior of additively manufactured 316L stainless steel. Materials. https://doi.org/10.3390/ma13153293
28. Afkhami S, Dabiri M, Piili H, Björk T (2021) Effects of manufacturing parameters and mechanical post-processing on stainless steel 316L processed by laser powder bed fusion. Mater Sci Eng A 802:140660
29. Rautio T et al (2022) The effect of severe shot peening on fatigue life of laser powder bed fusion manufactured 316L stainless steel. Materials. https://doi.org/10.3390/ma15103517
30. Elangeswaran C et al (2019) Effect of post-treatments on the fatigue behaviour of 316L stainless steel manufactured by laser powder bed fusion. Int J Fatigue 123:31–39
31. Lai W-J, Ojha A, Li Z, Engler-Pinto C, Su X (2021) Effect of residual stress on fatigue strength of 316L stainless steel produced by laser powder bed fusion process. Prog Addit Manuf 6:375–383
32. Gundgire T, Santa-aho S, Rautio T, Järvenpää A, Vippola M (2024) Synergistic effects of heat treatments and severe shot peening on residual stresses and microstructure in 316L stainless

steel produced by laser powder bed fusion. J Mater Process Technol. https://doi.org/10.1016/j.jmatprotec.2023.118229

33. Salman OO, Gammer C, Chaubey AK, Eckert J, Scudino S (2019) Effect of heat treatment on microstructure and mechanical properties of 316L steel synthesized by selective laser melting. Mater Sci Eng A 748:205–212
34. Qiu C, Adkins NJE, Attallah MM (2013) Microstructure and tensile properties of selectively laser-melted and of HIPed laser-melted Ti–6Al–4V. Mater Sci Eng A 578:230–239
35. Peters JO, Ritchie RO (2000) Influence of foreign-object damage on crack initiation and early crack growth during high-cycle fatigue of Ti–6Al–4V. Eng Fract Mech 67:193–207